Supplementary Information for

Aharonov–Bohm Interference in Even-Denominator Fractional Quantum Hall States

Contents

SI1 Device characterization

Fig. S1a shows the optical microscope image of the fabricated device for the current studies and Fig. S1b its scanning electron microscopic image. The scale bar is 200 nm. The red dashed hexagon shows the lithographic area of the Fabry-Pérot interference loop, which is A =1.0 μm^2. To characterize the quality of the device, we measured the carrier mobility of the fabricated device in a Hall bar geometry. Fig. S1c shows the two-probe resistance $R_{2\mathrm{p}}$, incorporating the contact resistance R_{c} as a function of V_{BG} while applying 5 nA at 0.1 K and $B = 0$ T. To extract the mobility μ we fit the measured $R_{2\mathrm{P}}$ to

$$R_{2p} = R_c + \frac{L}{W} \cdot \frac{1}{\mu\sqrt{e^2 n_0^2 + C_{\mathrm{BG}}^2 (V_{\mathrm{BG}} - V_{\mathrm{CNP}})^2}}. \tag{S1}$$

Here, n_0 denotes the intrinsic carrier concentration induced by substrate doping, C_{BG} is the capacitance per unit area of the bottom graphite gate, V_{CNP} is the voltage corresponding to the charge neutrality point, and L and W are the length between the two probe contacts and width of the Hall bar channel, and e the electron charge.[1]

By fitting to Eq. (S1), we obtained a high electron-mobility of $\mu \approx 1.23 \times 10^6$ cm^{-2}. Additionally, the intrinsic carrier concentration was found to be $n_0 = 1.4 \times 10^{-8}$ cm^{-2}, indicating a low charge carrier impurity density in our FPI device. In Fig. S1d, to confirm that the active layer consists of bilayer graphene, we observed its gap opening as a function of displacement field by measuring the two-probe resistance as a function of top gate voltage (V_{TG}) and bottom gate voltage (V_{BG}). As we move away from the charge neutrality point, the observed increase in resistance demonstrates the band gap opening in the bilayer graphene.

Following the low-field measurement to characterize the sample quality, we move on to characterize the device at high magnetic fields. Under the application of a magnetic field, 2D electrons in the bilayer are described by discrete Landau labels. When kinetic energy is quenched, electron interaction becomes crucial and gives rise to many incompressible states, such as the Fractional quantum Hall effect. We measure R_{xx} as a function of top gate voltage (V_{TG}) and magnetic field (B) at a fixed back gate voltage (V_{TG}) of 0.65 V at B = 11 T and 10 mK. We observe a rich fan diagram showing a series of even and odd fractional quantum Hall (FQH) states on both electron and hole sides, as shown in Fig. S1e,f, and consistent with earlier studies.[2,3] We observe between $\nu = 1, 2$ and between $\nu = -1, 0$, a half-filled plateau and few Jain states (near $D = 0$) while between $\nu = 0, 1$ and between $\nu = -2, 1$ there is no plateau at half-filled and many Jain states shown in Fig. S1e,f.

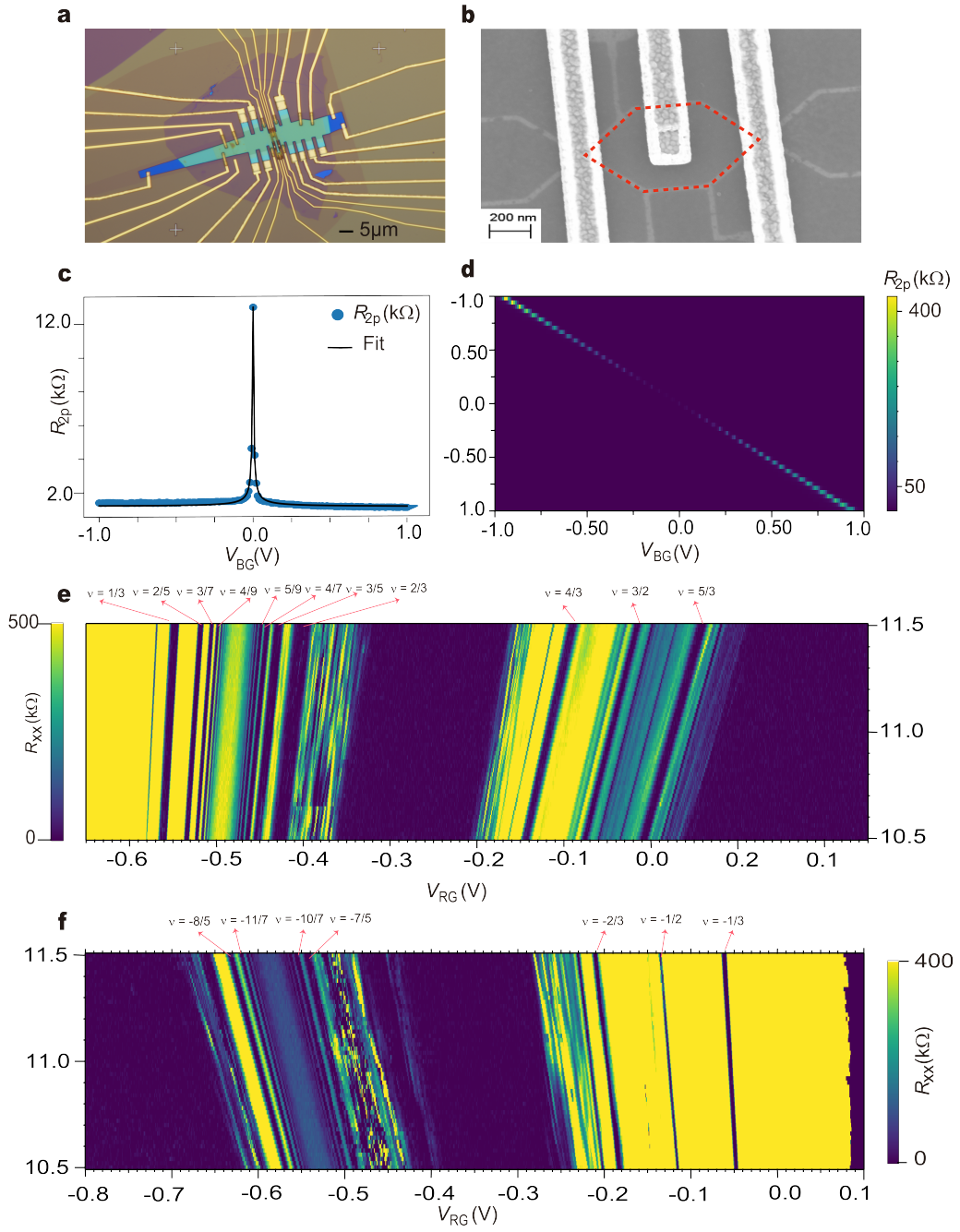

Figure S1: Device Characterization (**a**) Optical image of a bilayer graphene-based FPI. Scale bar 5μm (**b**) Scanning electron microscope image of the device, where the red dashed line shows an interference loop area of 1 μm^2. Scale bar 200nm (**c**) Two-probe resistance R_{2p} as a function of V_{BG}, measured by applying a 5 nA current at 1 K under a magnetic field of 0 T. (**d**) R_{2p} as a function of top and bottom gate voltage showing a clear gap opening in bilayer graphene, measured at 1 K at 0 T magnetic field. (**e**) R_{xx} is measured at 10 mK and at 11 T with a fixed Si = 5 V and V_{BG} = 0.65 V with 1 nA current applied. (**f**) R_{xx} is measured at 10 mK and at 11 T with a fixed Si = -5 V and V_{BG} = -0.1 V with 1 nA current applied.

SI2 Extracting α_c from longitudinal resistance measurement

In this section, we briefly discuss the extraction of α_c values for different even and odd denominator fractional quantum Hall states. A 2D map of R_{xx} is measured as a function of V_{RG} at the base temperature of 10 mK between 10.5 T and 11.5 T as shown in Fig. 2b,e in the main text. To find the value of α_c's, from the 2D map, we take line cuts at two different magnetic fields, 10.5 T and 11.5 T. As shown in Fig. 2b,e, within the boundaries marked by the red dashed lines, we extract the slope of the constant filling line at the center of the R_{xx} dip, which provides the values of α_c's.

Determination of α_c for hole and electron carriers: In Fig. S2a,b, we present fully developed FQH states measured at magnetic fields of 10.5 T and 11.5 T on the hole-doped and electron-doped sides, respectively.

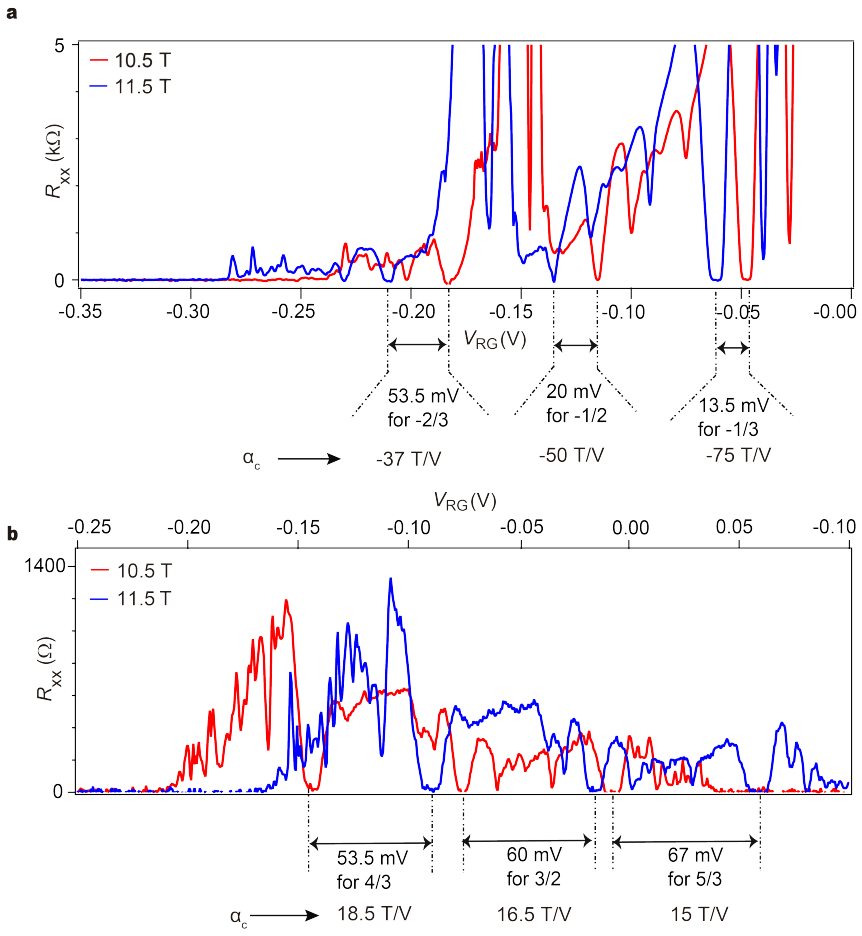

Figure S2: Determination of α_C values. (a) Line cuts of R_{xx} as a function of V_{RG} at magnetic fields of 10.5 T (red) and 11.5 T (blue) for hole carriers. **(b)** Same as (a), but for electron carriers.

We determine the shift in gate voltage, δV_{RG}, by calculating the difference between the positions of

two vertical dashed lines drawn at the center of the plateaus where R_{xx} drops to zero for FQH states. For hole carriers, this corresponds to $\nu = -\frac{2}{3}$, $-\frac{1}{2}$, and $-\frac{1}{3}$ (Fig. S2a) and , and for electron carriers, $\nu = \frac{4}{3}$, $\frac{3}{2}$, and $\frac{5}{3}$ (Fig. S2b). The magnetic field difference, δB, is defined as the separation between the two magnetic field values at which the longitudinal resistance line cuts are taken. We then calculate $\alpha_c = \frac{\delta B}{\delta V_{\mathrm{RG}}}$. For hole carriers, the FQHE states at $\nu = -\frac{2}{3}$, $-\frac{1}{2}$, and $-\frac{1}{3}$ yield α_c values of, -37 T/V, -50 T/V, and -75 T/V, respectively. For electron carriers, the FQHE states at $\nu = \frac{4}{3}$, $\frac{3}{2}$, and $\frac{5}{3}$ results in α_c values of 18.5 T/V, 16.5 T/V, and 15 T/V, respectively. From the Streda formula, $C_{\mathrm{RG}} = \frac{e\alpha_c\nu}{\Phi_0}$, the capacitance of the right gate (RG) per unit area is calculated as $C_{\mathrm{RG}} = 0.959$ mF/m^2 using the average value of $\alpha_c\nu$ for all fractional fillings, different from the value of C_{CG} discussed in Sec. SI12.

SI3 Electron carrier Aharonov-Bohm oscillations

In this section, we show diagonal resistance, R_{D}, as a function of plunger gate voltage, V_{PG}, measured at a constant magnetic field and a base temperature of 10 mK, with a source-drain current of 500 pA. This analysis is performed for both integer and fractional quantum Hall states on the electron-doped side. The quantum point contact (QPC) transmissions are maintained at approximately 50% for integers and 70–80% for fractional edge modes.

We set $\nu = 1$, $\frac{3}{2}$, $\frac{4}{3}$, and $\frac{5}{3}$ in the LG, CG, and RG regions and observe stable resistance oscillations as a function of the plunger gate voltage, V_{PG}. To estimate the visibility of the inner or outer edge modes, we use the following equation

$$\mathrm{Visibility} = \frac{G_{\max} - G_{\min}}{G_{\max} + G_{\min} - 2 \cdot G_{\nu_{\mathrm{outer}}}}, \tag{S2}$$

where $G_{\max}$ and $G_{\min}$, are the maximum and minimum diagonal conductance values, and $G_{\nu_{\mathrm{outer}}}$ represents the conductance of a fully transmitted outer edge mode. The visibilities of the oscillations for $\nu = 1$, $\frac{3}{2}$, $\frac{4}{3}$, $\frac{5}{3}$ are roughly estimated to be 9.5%, 5.6%, 11.8%, 4.5% as shown in Fig. S3a-d. Notably, the hole-conjugate state at $\nu = \frac{5}{3}$ exhibits significantly lower visibility compared to the $\nu = \frac{4}{3}$ fractional quantum Hall state. One possible explanation for this difference is the distribution of current among multiple edge modes, with potentially only one mode contributing to interference. However, the primary reason for the lower visibility at $\nu = \frac{5}{3}$ compared to $\nu = \frac{4}{3}$ remains unclear.[4]

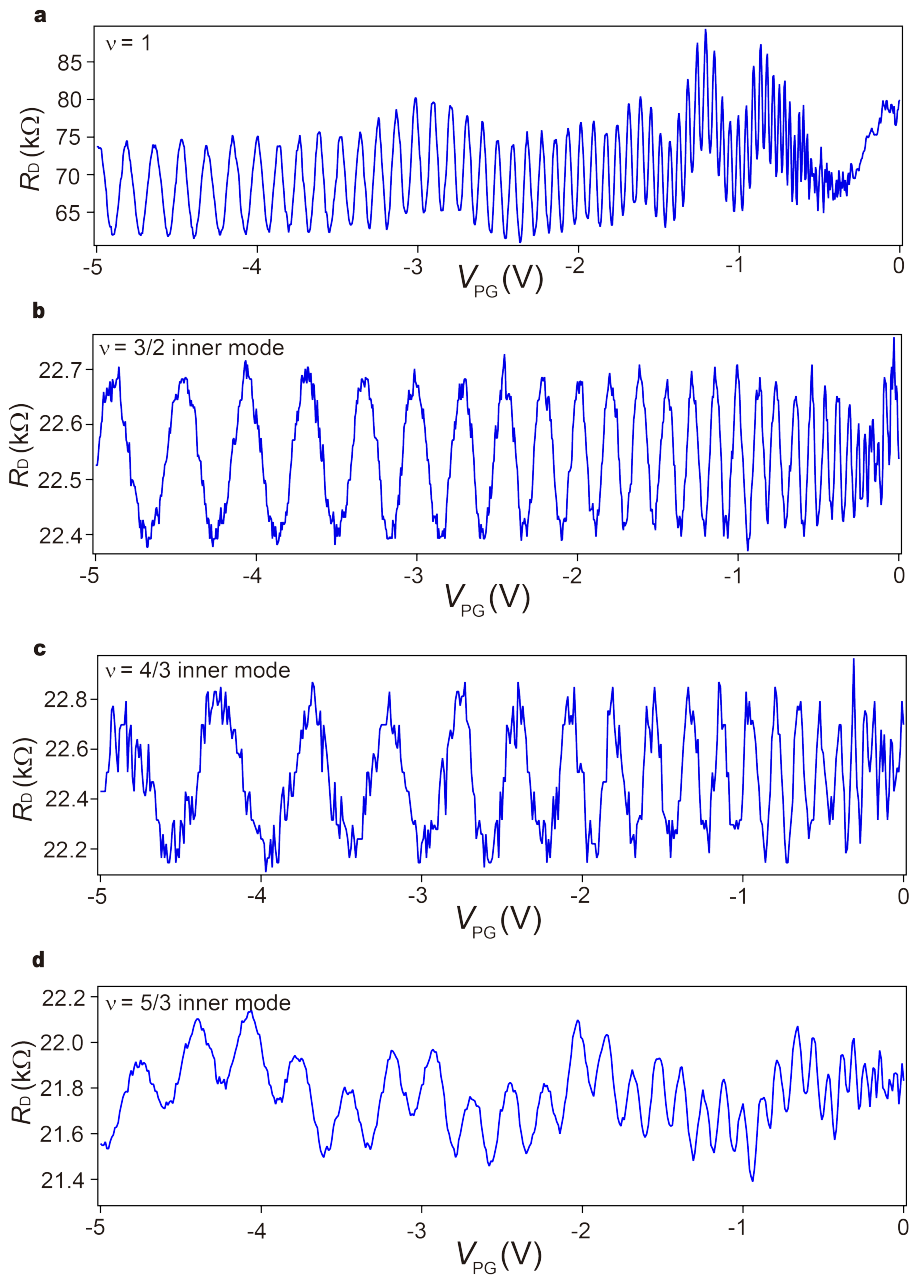

Figure S3: Aharonov-Bohm oscillations as a function plunger gate voltage: (**a-d**) Diagonal resistance measured as a function of plunger gate voltage for electron carriers for (a) $\nu = 1$, (b) $\nu = \frac{3}{2}$ inner mode, (c) $\nu = \frac{4}{3}$ inner mode, and (d) $\nu = \frac{5}{3}$ inner mode.

SI4 Hole carrier Aharonov-Bohm oscillations

For hole carriers, we measure the diagonal resistance, R_{D}, as a function of plunger gate voltage, V_{PG}, at a constant magnetic field and a temperature of 10 mK, with a source-drain current of 100 pA. Figure S4a–e presents conductance oscillations for $\nu = -1$, $-\frac{1}{2}$, $-\frac{1}{3}$, $-\frac{2}{3}$, and -2, yielding visibilities of 2.3%, 1.9%, 2.3%, 0.7%, and 33.5%, respectively, using the formula defined in SI3. Similar to the electron-doped region, the diagonal resistance oscillations exhibit lower visibility for the particle-conjugate state $\nu = -\frac{2}{3}$ compared to the $\nu = -\frac{1}{3}$ fractional quantum Hall state.

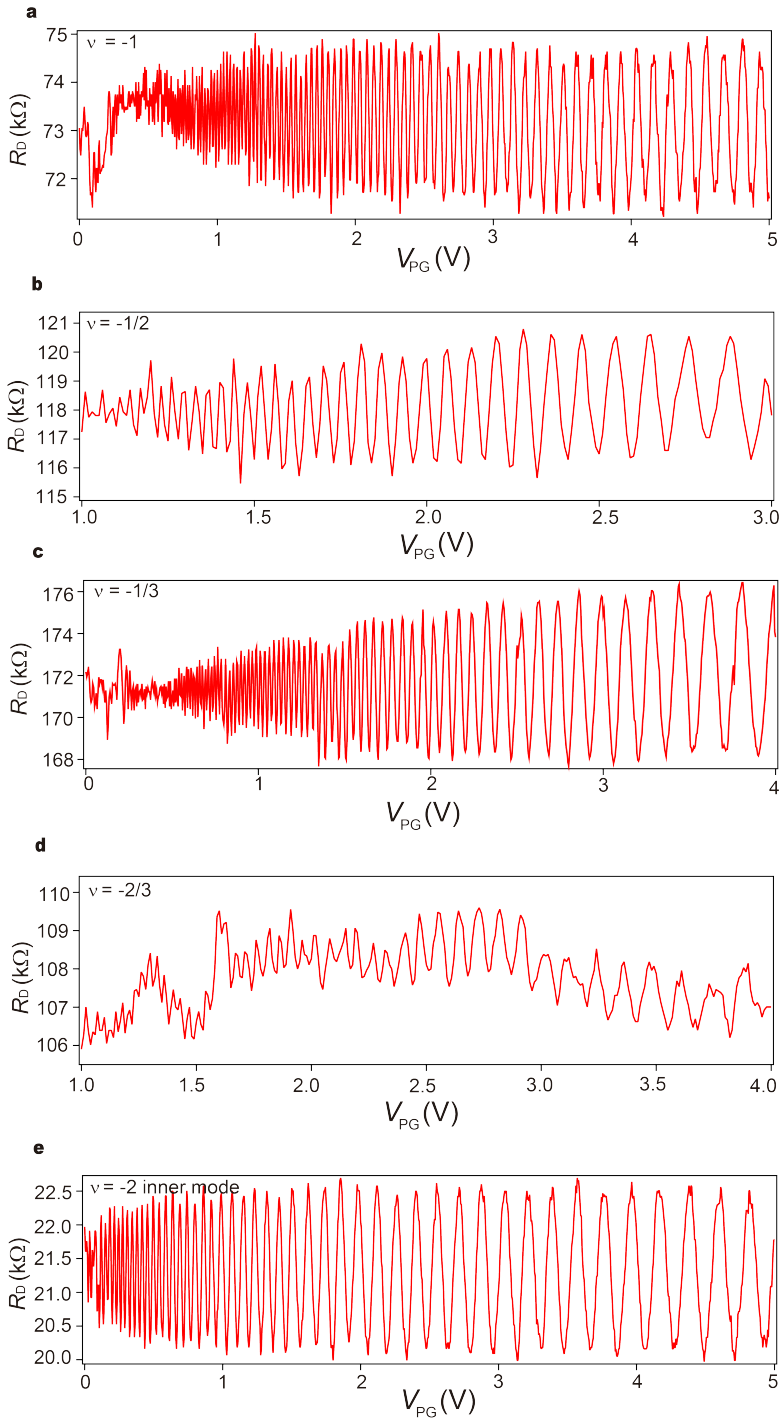

Figure S4: Aharonov-Bohm oscillations as a function plunger gate voltage (**a-e**) Diagonal resistance measured as a function of plunger gate voltage for the hole carriers for (a) $\nu = -1$, (b) $\nu = -\frac{1}{2}$, (c) $\nu = -\frac{1}{3}$, (d) $\nu = -\frac{2}{3}$, (e) $\nu = -2$ inner mode.

SI5 1D-FFT analysis for the phase jump at $\nu = -\frac{1}{3}$

Fig. S5a shows diagonal resistance measurements as a function of the plunger gate voltage, V_{PG}, and the central gate voltage, V_{CG}, for $\alpha_c = 0$ at 11 T and 10 mK. In Fig. S5b, we focus on the region highlighted by the black dashed window, where a distinct series of phase slips is observed, corresponding to the addition or removal of charged quasiparticles. We perform 1D-FFTs of ΔR_{D} for fixed values of V_{CG} to extract the magnitude of the phase jumps based on the phase at the 1D-FFT peak. To ensure a continuous phase evolution and avoid discontinuities at $\pm\pi$ as a function of V_{CG}, a 2π phase shift is added as necessary. The magnitude of the phase slips $\frac{\Delta\theta}{2\pi}$, are calculated by taking a difference between the average values on two adjacent AB regions after deducting the global AB contribution as shown in Fig. S5c. This analysis yields an average phase slip value of $\frac{\Delta\theta}{2\pi} = 0.30 \pm 0.03$, which is consistent with the theoretically expected value of $\theta_{\mathrm{anyon}} = \frac{2\pi}{3}$.

The deviations in the values of the measured phase slips can arise from to bulk-edge coupling [5]

$$\frac{\Delta\theta}{2\pi} = -\frac{\theta_{\mathrm{anyon}}}{2\pi} + 3\frac{K_{\mathrm{IL}}}{K_{\mathrm{I}}}\left(\frac{e^*}{e}\right)^2, \tag{S3}$$

where K_{IL} is the bulk-to-edge coupling, and K_{I} is the edge stiffness describing the energy cost to vary the interfering area A. According to Eq. (S3), the magnitude of the phase slips can vary when a non-negligible K_{IL} exists, explaining that the majority of the observed phase slips are smaller than $\frac{2\pi}{3}$.[5,6] Moreover, the behavior of different $\frac{\Delta\theta}{2\pi}$ may be ascribed to the case in which both K_{IL} and K_{IL} can be affected by the number of bulk quasiparticles.

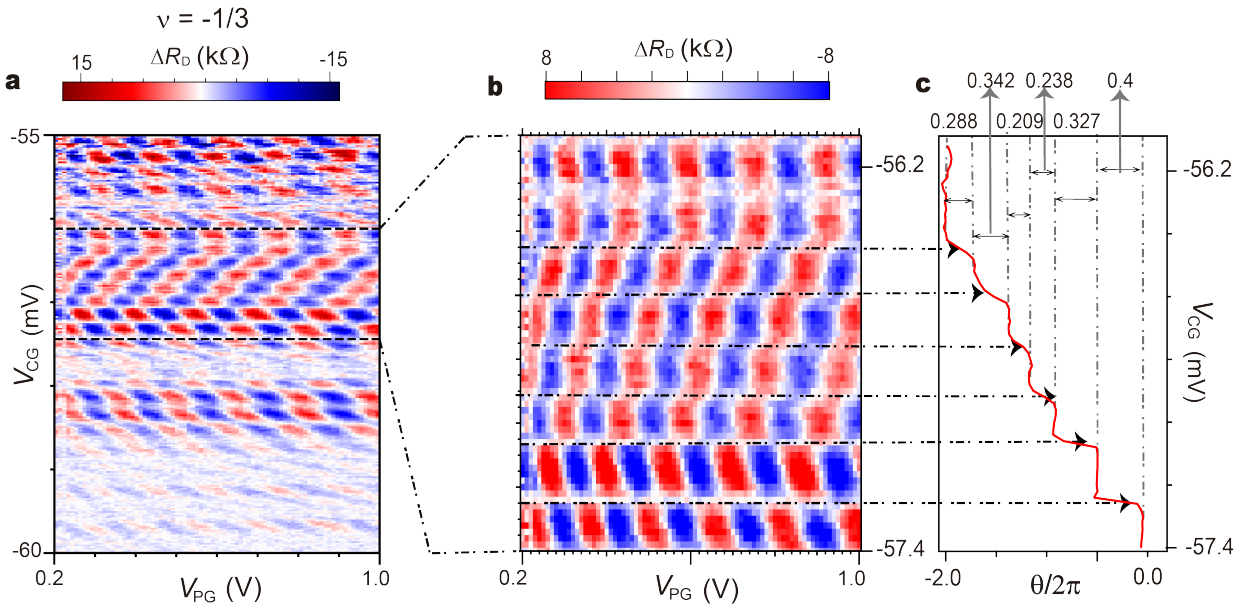

Figure S5: 1D-FFT analysis for the phase jump for $\alpha = 0$ (**a**) ΔR_{D} is measured for $\nu = -\frac{1}{3}$ as function of $\mathrm{V_{CG}}$ and $\mathrm{V_{PG}}$ at 10 mK (**b**) A small window of ΔR_{D} from Fig. S5a where a series of phase slips occur. (**c**) $\frac{\theta}{2\pi}$ plotted as function of V_{CG} with subtraction of the global Aharonov-Bohm contribution.

SI6 Aharonov–Bohm interference in hole-doped odd- and even-denominator FQH states

Figs. S6a-d, show R_{D} measurements plotted in $B|_{\alpha_c}$-V_{PG} planes corresponding to filling factors of $\nu = -1$, $-\frac{2}{3}$, $-\frac{1}{2}$, and $-\frac{1}{3}$. For all fillings, clear AB-dominated interference patterns are observed. For hole doping, constant-phase lines in the AB regime are expected to exhibit positive slopes, in contrast to the negative slopes observed for electron doping. We observe a change in the R_{D} background as a function of V_{CG}, which can be attributed to the change in the transmission of the QPCs. Figs. S6e-h present the 2D-FFTs of the corresponding data in Figs. S6a-d, respectively, plotted as a function of $\frac{\Phi_0}{\Delta B}$ and $\frac{1}{\Delta V_{\mathrm{PG}}}$. We extract the interference area of 1.02 $\mu\mathrm{m}^2$ for $\nu = -1$, assuming an interfering charge of e. This is in good agreement with the lithographic area of the center gate (CG) estimated to be 1 $\mu\mathrm{m}^2$.

To determine the magnetic field periodicity ΔB, we analyze one-dimensional cuts of the 2D-FFT as a function of $\frac{\Phi_0}{\Delta B}$, taken at the peak value of ΔV_{PG}. Figs. S6i-l show these FFT amplitude line curves as a function of $\frac{\Phi_0}{\Delta B}$. By fitting a Gaussian curve to the data, we extract the mean value $\frac{\Phi_0}{\Delta B_{\mathrm{fit}}}$ and the variance σ^2, as shown in the lower-right sides of Figs. S6i-l.

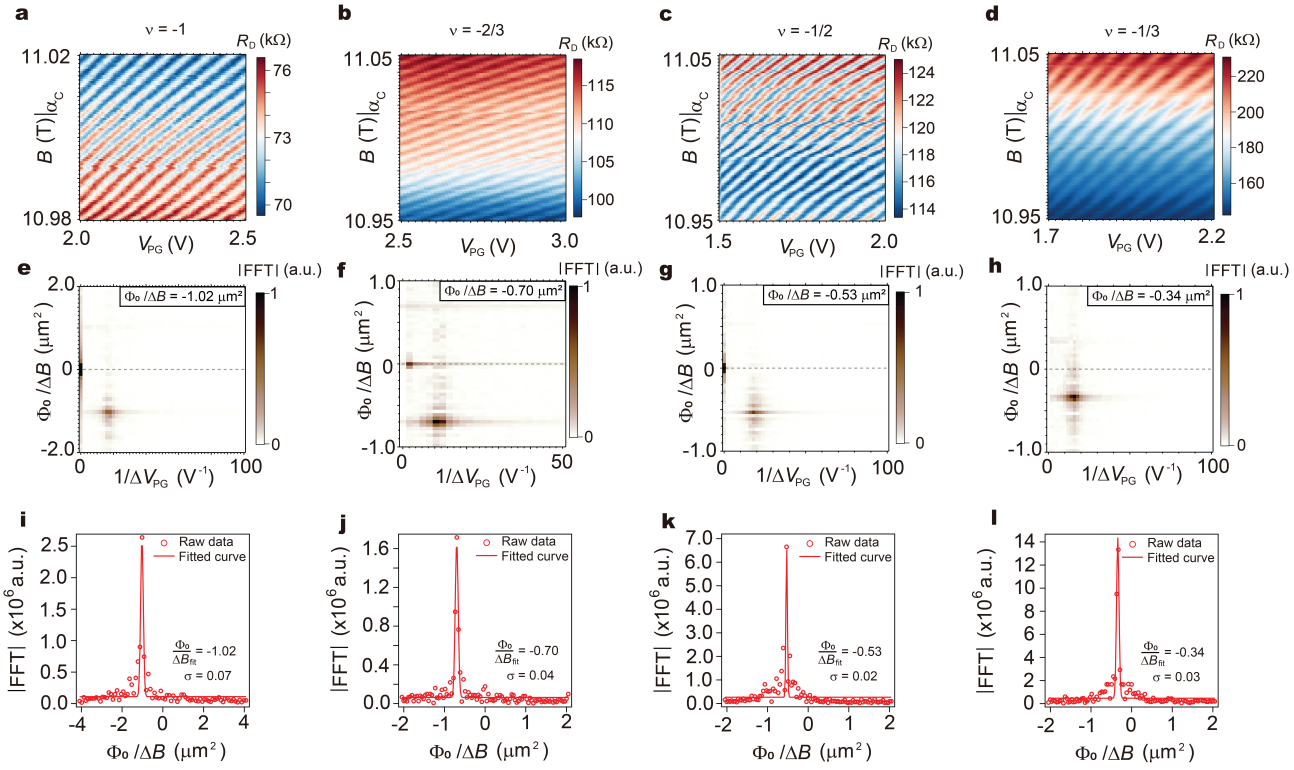

Figure S6: Hole-doped Aharonov–Bohm interference. (**a-d**) R_{D} for $\nu = -1, -\frac{2}{3}, -\frac{1}{2}$, and $-\frac{1}{3}$, measured in $B|_{\alpha_c}$-V_{PG} plane. (**e-h**) 2D-FFT as a function of $\frac{\Phi_0}{\Delta B}$ and $\frac{1}{\Delta V_{\mathrm{PG}}}$, corresponding to Figs. S6a-d, respectively. (**i-l**) 1D cuts of the 2D-FFT as a function of $\frac{\Phi_0}{\Delta B}$, taken at the peak value of ΔV_{PG}, obtained from Figs. S6e-h, respectively. Lower-right sides: Gaussian fitting parameters.

SI7 Aharonov–Bohm interference in electron-doped odd- and even-denominator FQH states

Figs. S7a-e show AB pajamas at constant filling for $\nu = 1$ and the inner modes of $\nu = \frac{4}{3}, \frac{3}{2}, \frac{5}{3}, 2$. For all filling factors, clear AB-dominated interference patterns with negative slopes of the constant-phase lines are observed, consistent with expectations for electron doping. Figs. S7f-j present the corresponding 2D-FFTs of the data shown in Figs. S7a-e, respectively, plotted as a function of $\frac{\Phi_0}{\Delta B}$ and $\frac{1}{\Delta V_{\mathrm{PG}}}$. For the integer filling factors $\nu = 1$ and 2, where the interfering charge is expected to be e, the interfering area A is extracted from the 2D-FFTs shown in Figs. S7f and S7j. This provides upper and lower bounds for A for intermediate filling factors between $1 < \nu < 2$. Averaging these bounds yields an interfering area of $A = 0.99 \pm 0.10$ $\mu\mathrm{m}^2$.

To determine the magnetic field periodicity ΔB, we proceed as in Sec. SI6. Figs. S7k-o show 1D-FFT amplitudes as a function of $\frac{\Phi_0}{\Delta B}$, taken at the peak value of ΔV_{PG}. By fitting a Gaussian curve to the data, we extract the mean value $\frac{\Phi_0}{\Delta B_{\mathrm{fit}}}$ and the variance σ^2, as shown in the lower-right sides of Figs. S7k-o.

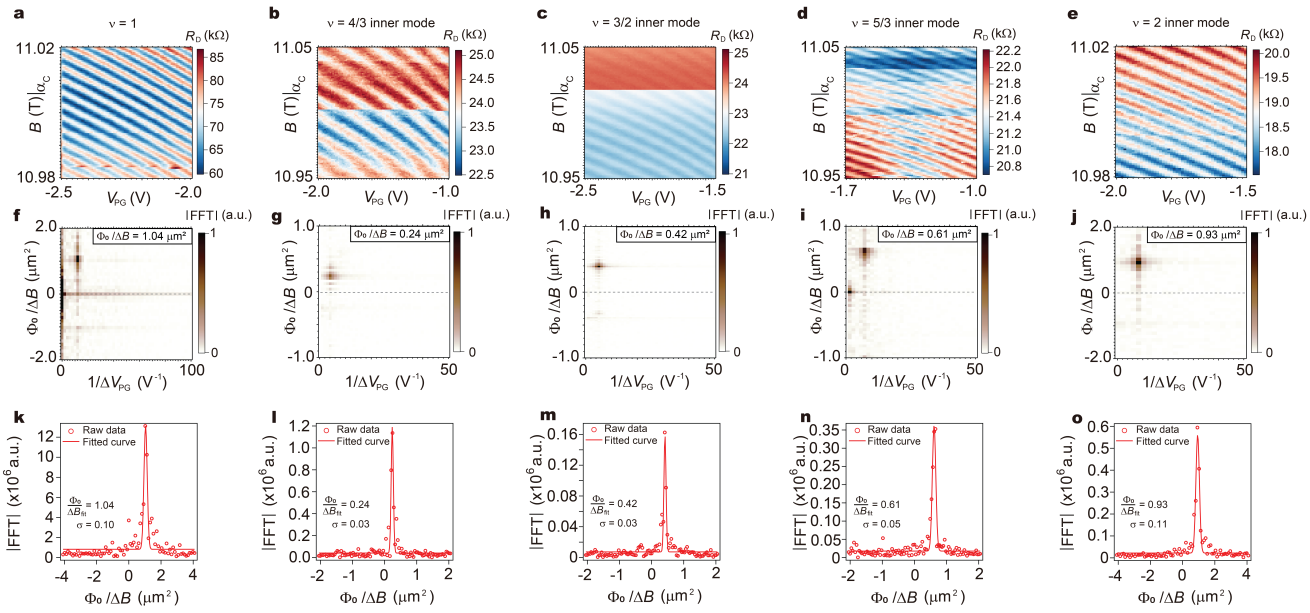

Figure S7: Electron-doped Aharonov–Bohm interference. (**a-e**) R_{D} for $\nu = 1$, $\frac{4}{3}$ inner mode, $\frac{3}{2}$ inner mode, $\frac{5}{3}$ inner mode, and 2 inner mode, measured in $B|_{\alpha_c}$-V_{PG} plane. (**f-j**) 2D-FFT as a function of $\frac{\Phi_0}{\Delta B}$ and $\frac{1}{\Delta V_{\mathrm{PG}}}$, corresponding to Figs. S7a-e, respectively. (**k-o**) 1D cuts of the 2D-FFT as a function of $\frac{\Phi_0}{\Delta B}$, taken at the peak value of ΔV_{PG}, obtained from Figs. S7f-j, respectively. Lower-left sides: Gaussian fitting parameters.

SI8 Temperature dependence on resistance oscillations for $\nu = -\frac{1}{2}$

Here, we show $\Delta R_{\rm D}$ for $\nu = -\frac{1}{2}$, measured in the $B|_{\alpha_c}$-$V_{\rm PG}$ plane at temperatures of 10 mK, 50 mK, 80 mK, and 100 mK. As expected, the visibility decreases with increasing temperature due to the dephasing of the interfering quasiparticle. The magnetic-field periodicity, shown in the insets of Figs. S8a-d, does not change over the entire temperature range.

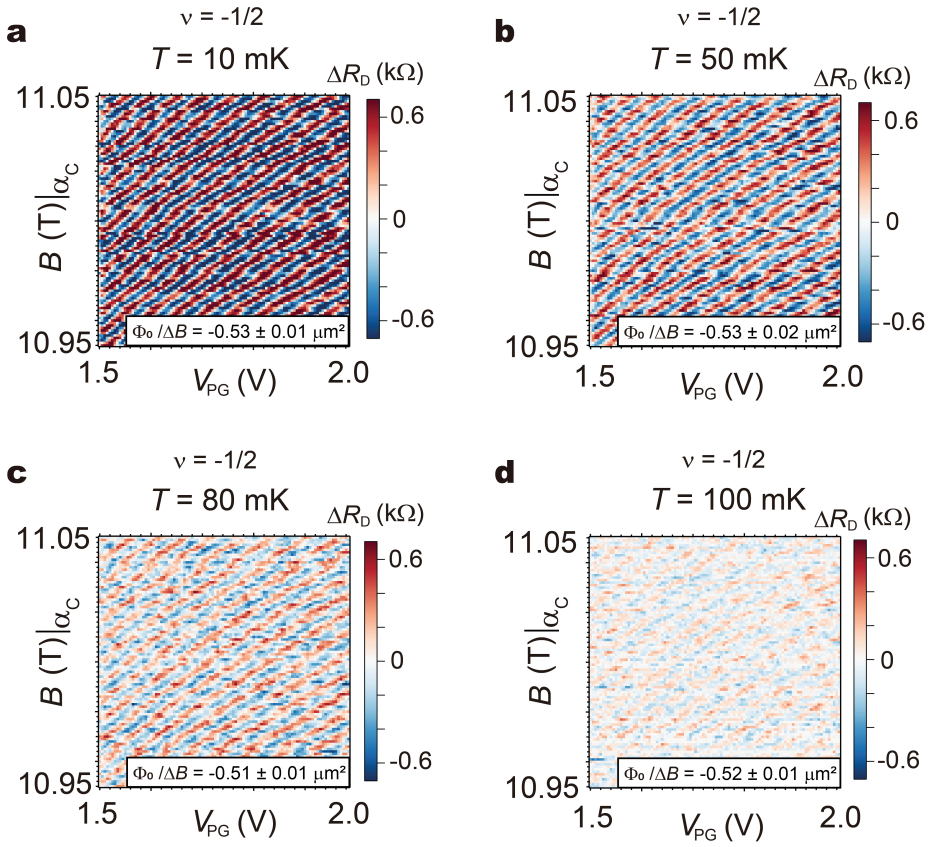

Figure S8: Temperature dependent Aharonov-Bohm interference for $\nu = -\frac{1}{2}$. (**a-d**) $\Delta R_{\rm D}$ at $\nu = -\frac{1}{2}$ displayed in $B|_{\alpha_c}$-$V_{\rm PG}$ plane for different temperatures, (a) T = 10 mK, (b) T = 50mK, (c) T = 80 mK, and (d) T = 100 mK. α_c = -50 T/V is obtained using $C_{\rm RG}$ calculated in Sec. SI2

SI9 Temperature dependence on resistance oscillations for $\nu = \frac{3}{2}$

As in the previous section, we present ΔR_{D} measurements for $\nu = \frac{3}{2}$, focusing on the interfering fractional inner edge mode attemperatures of 10 mK, 20 mK, 30 mK, and 50 mK. For these measurements, an α_c value of 15.3 T/V is chosen, resulting in $\Delta\Phi = (2.01 \pm 0.35)\Phi_0 \approx 2\Phi_0$ at 10 mK. As shown in Figs. S9a-d, the magnetic-field periodicity remains constant over this temperature range. However, in this case, visibility is lost above the lower temperature of 50 mK.

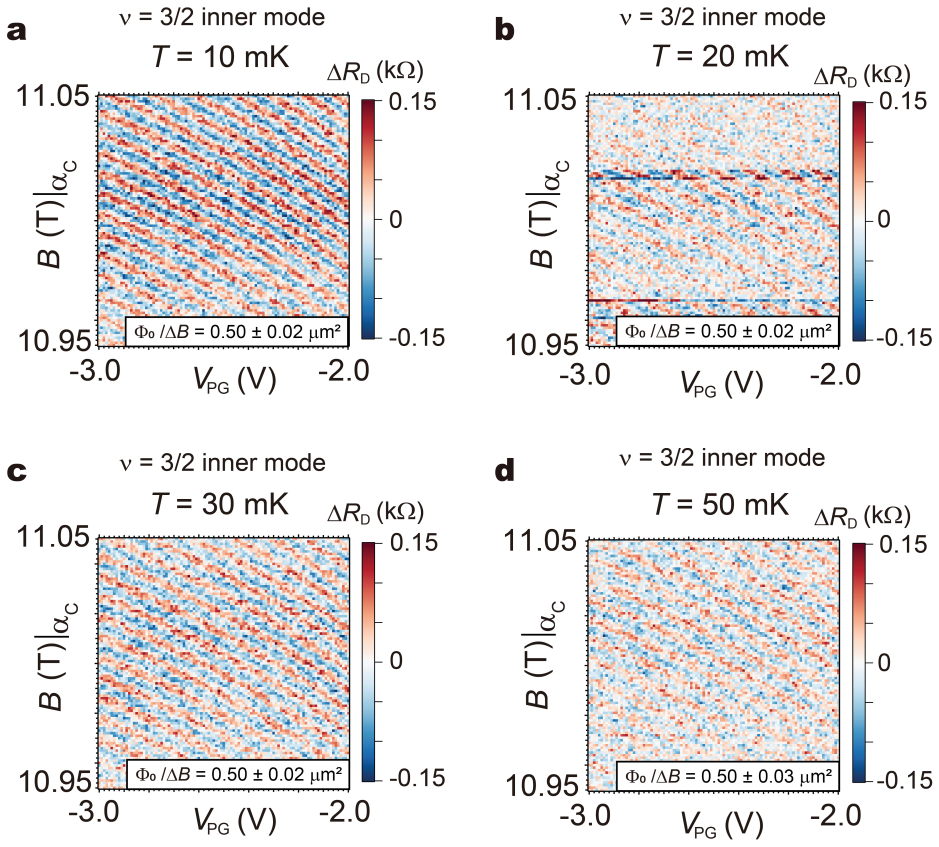

Figure S9: Temperature dependent Aharonov-Bohm interference for $\nu = \frac{3}{2}$ inner mode. (**a-d**) ΔR_{D} at $\nu = \frac{3}{2}$ inner mode displayed in $B|_{\alpha_c}$-V_{PG} plane for different temperatures, (a) T = 10 mK, (b) T = 20mK, (c) T = 30 mK, and (d) T = 50 mK. α_c = 15.3 T/V is obtained using C_{CG} calculated in Sec. SI12.

SI10 Aharonov-Bohm interference for $\nu = \frac{3}{2}$ outer mode

At the bulk filling $\nu = \frac{3}{2}$, we also measured interference of the integer outer mode. The AB pajama in Fig. S10a and its 2D-FFT in Fig. S10b yield $\frac{\Phi_0}{\Delta B}$ =1.11 μm^2, consistent with an interfering charge e. It also indicates that the interference area is slightly larger than for the inner-mode interference, as expected.

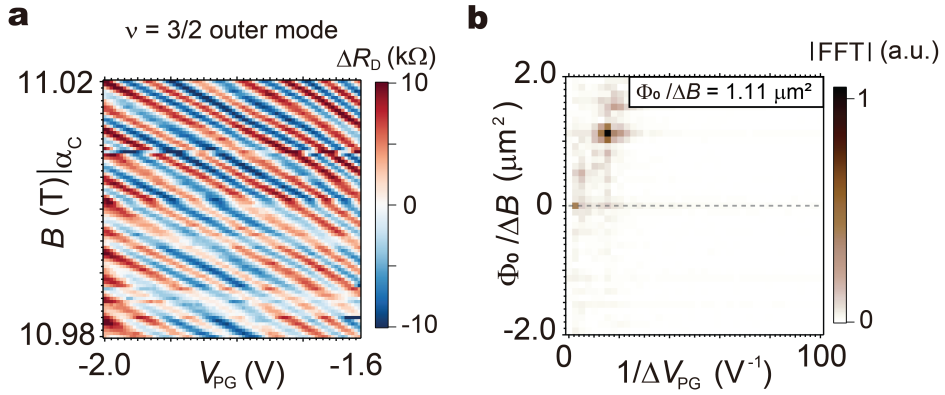

Figure S10: Aharonov-Bohm interference for the outer mode of $\nu = \frac{3}{2}$. (**a**) $\Delta R_{\rm D}$ at $\nu = \frac{3}{2}$ displayed in $B|_{\alpha_c}$-$V_{\rm PG}$ plane, with partitioning of the integer outer mode. (**b**) Corresponding 2D-FFT analysis used to extract the magnetic field periodicity $\frac{\Phi_0}{\Delta B}$.

SI11 Derivation of the statistical contribution to the magnetic-field periodicity

As discussed in the main text, the diagonal resistance $R_{\mathrm{D}} = \frac{V_{\mathrm{D}}{}^{+} - V_{\mathrm{D}}{}^{-}}{I_{\mathrm{SD}}}$ includes an oscillatory contribution $\Delta R_{\mathrm{D}} \propto \cos\theta$, with the interference phase θ as given in Eq. (1) in the main text. In particular, this phase depends on the number N_2 of localized quasiparticles inside the interference loop. It is plausible that, in the course of the measurement, this number fluctuates. In this section, we compute the average of the oscillatory term $\langle \Delta R_D \rangle$ over this number. The phase θ is given by

$$\theta = 2\pi \left(\frac{e_1^*}{e} \frac{AB}{\Phi_0} + \frac{\theta_{12}}{2\pi} N_2 \right) \tag{S4}$$

with e_1^* the interfering quasiparticle charge, e_2^* the charge of localized quasiparticles, and θ_{12} is the statistical phase of e_1^* encircling e_2^*. The interferometer area A is assumed constant throughout this analysis.

The average oscillatory term is given by

$$\langle \Delta R_D \rangle \ = \sum_{N_2} P(N_2) \cos \left[2\pi \left(\frac{e_1^*}{e} \frac{AB}{\Phi_0} + \frac{\theta_{12}}{2\pi} N_2 \right) \right] \ , \tag{S5}$$

where $P(N_2)$ is the probability distribution of N_2. We will treat N_2 as a discrete random variable with a Gaussian distribution with mean $\langle N_2 \rangle$ and variance σ, i.e.,

$$P\left(N_2\right) = \mathcal{N} \exp \left[-\frac{\left(N_2 - \langle N_2 \rangle\right)^2}{2\sigma^2} \right] \ , \tag{S6}$$

with $\mathcal{N}$ a normalization constant. The average number of quasiparticles, $\langle N_2 \rangle$, depends continuously on the electron density and magnetic field and is not required to be an integer. To evaluate the average, we employ the Poisson summation formula to write

$$\langle \Delta R_D \rangle = \mathcal{N} \sum_s \int_{-\infty}^{\infty} dN_2 \exp \left[-i2\pi s N_2 - \frac{\left(N_2 - \langle N_2 \rangle\right)^2}{2\sigma^2} \right] \cos \left[2\pi i \left(\frac{e_1^*}{e} \frac{AB}{\Phi_0} + \frac{\theta_{12}}{2\pi} N_2 \right) \right] . \tag{S7}$$

Performing the Gaussian integral over N_2, we obtain

$$\langle \Delta R_D \rangle = \sqrt{2\pi\sigma} \mathcal{N} \sum_s e^{-\frac{\sigma^2}{2}(\theta_{12} - 2\pi s)^2} \cos \left[2\pi \frac{e_1^*}{e} \frac{AB}{\Phi_0} + \left(\theta_{12} - 2\pi s\right) \langle N_2 \rangle \right] . \tag{S8}$$

For $\sigma^2 \gtrsim 1$, the sum is dominated by the integers that minimize $\left(\theta_{12} - 2\pi s\right)^2$. We begin with $\theta_{12} \neq (2n+1)\pi$, for which there is a single dominant integer s_0. Keeping only the corresponding term we obtain

$$\langle \Delta R_D \rangle \approx e^{-\frac{\sigma^2}{2}(\theta_{12} - 2\pi s)^2} \cos \left[2\pi \frac{e_1^*}{e} \frac{AB}{\Phi_0} + \left(\theta_{12} - 2\pi s_0\right) \langle N_2 \rangle \right] . \tag{S9}$$

Next, we compute the average $\langle N_2 \rangle$. We define ν as the 'pristine' filling factor, i.e., the rational number defining the FQH plateau. When the magnetic field B and electron number N satisfy $N = \nu \frac{AB}{\Phi_0}$,

there are no quasiparticles in the ground state. Deviations from the relation via $B \to B + \Delta B$ or $N \to N + \Delta N$ introduce a number of charge e_2^* quasiparticles given by

$$e_2^* \langle N_2 \rangle = e\Delta N + \frac{e\nu A}{\Phi_0}\Delta B \,. \tag{S10}$$

The first term on the right-hand side corresponds to the charge entering the interfering loop due to the change in V_{CG}, i.e., $e\Delta N = CA\Delta V_{CG}$ with C the CG capacitance per unit area. The second term encodes excitations that arise as the change in the magnetic field modifies the Landau-level degeneracy.

In the experiment, the interference pattern was recorded along specific lines in the B–V_{CG} plane parameterized by $\alpha = \frac{\partial B}{\partial V_{CG}}$. Along such trajectories, ΔN and ΔB are related via $\Delta N = \frac{CA}{e\alpha}\Delta B$. and the average number of quasiparticles is thus given by

$$\langle N_2 \rangle = \frac{e}{e_2^*}\left(\frac{CA}{e}\frac{1}{\alpha} - \frac{\nu A}{\Phi_0}\right)\Delta B \,. \tag{S11}$$

Inserting this average into Eq. (S9) we finally obtain, up to a constant phase inside the cosine,

$$\langle \Delta R_D \rangle \approx e^{-\frac{\sigma^2}{2}(\theta_{12}-2\pi s)^2} \cos\left[\left(2\pi\frac{e_1^*}{e} + (\theta_{12}-2\pi s_0)\frac{\nu e}{e_2^*}\frac{\alpha_c - \alpha}{\alpha}\right)\frac{A\Delta B}{\Phi_0}\right], \tag{S12}$$

where we used $\alpha_c = \frac{C\Phi_0}{\nu e}$. For $\alpha = \alpha_c$ we recover the pristine AB interference without quasiparticle contributions.

For the filling factors $\nu = \frac{4}{3}$ and $\frac{5}{3}$ with an interfering quasiparticle charge of $e_1^* = \nu_{LL} e$, we find a different ΔB dependence for bulk quasiparticles $e_2^* = \frac{1}{3}e$ or $e_2^* = \frac{2}{3}e$. The statistical phases for the two types of bulk quasiparticles are $\theta_{12} = \frac{2\pi}{3}$ (such that $s_0 = 0$) and $\frac{4\pi}{3}$ (such that $s_0 = -1$), respectively, i.e.,

$$e_2^* = \frac{1}{3} : \langle \Delta R_D \rangle_{\nu=\frac{4}{3},\frac{5}{3}} \approx e^{-\frac{2\sigma^2\pi^2}{9}} \cos\left[2\pi\left(\nu_{LL} - \nu + \nu\frac{\alpha_c}{\alpha}\right)\frac{A\Delta B}{\Phi_0}\right] \tag{S13}$$

$$e_2^* = \frac{2}{3} : \langle \Delta R_D \rangle_{\nu=\frac{4}{3},\frac{5}{3}} \approx e^{-\frac{2\sigma^2\pi^2}{9}} \cos\left[2\pi\left(\nu_{LL} - \nu - \nu\frac{\alpha_c}{\alpha}\right)\frac{A\Delta B}{\Phi_0}\right] \,. \tag{S14}$$

At $\nu = \frac{3}{2}$ we again take $e_1^* = \nu_{\mathrm{LL}} e$. For the bulk quasiparticles, we consider $e_2^* = \frac{1}{4}$ in which case $\theta_{12} = \frac{\pi}{2}$ or $e_2^* = \frac{1}{4}$, for which $\theta_{12} = \pi$. In the first case, the sum in Eq. (S8) is dominated by $s_0 = 0$, but in the second case, $s_0 = 0$ and $s_0 = 1$ contribute equally. Proceeding as before, we find

$$e_2^* = \frac{1}{2} : \langle \Delta R_D \rangle_{\nu=\frac{3}{2}} \approx 2e^{-\frac{\sigma^2\pi^2}{2}} \cos\left[2\pi\nu_{LL}\frac{A\Delta B}{\Phi_0}\right] \cos\left[2\pi\left(-\nu + \nu\frac{\alpha_c}{\alpha}\right)\frac{A\Delta B}{\Phi_0}\right] \,, \tag{S15}$$

$$e_2^* = \frac{1}{4} : \langle \Delta R_D \rangle_{\nu=\frac{3}{2}} \approx e^{-\frac{\sigma^2\pi^2}{8}} \cos\left[2\pi\left(\nu_{LL} - \nu + \nu\frac{\alpha_c}{\alpha}\right)\frac{A\Delta B}{\Phi_0}\right] \,. \tag{S16}$$

We note that double windings of the fundamental charge $e_1^* = \frac{1}{3}e$ or $\frac{1}{4}e$ would yield the same phase evolution as a single winding of twice that charge, and this analysis cannot distinguish between these two scenarios. In contrast, the charge of the localized quasiparticles, e_2^*, can be inferred by examining the slope of $\frac{\Phi_0}{\Delta B}$ as a function of $\frac{1}{\alpha}$. The data for $\nu = \frac{3}{2}, \frac{4}{3}, \frac{5}{3}$ (main text), and for $\nu = -\frac{1}{2}, -\frac{2}{3}$ (Fig. S11) follow the slope $\nu\alpha A$. In particular, at both half-filled states, there is a single periodicity, which is inconsistent with Eq. (S15). We conclude that in all the measured states, deviations of the filling factor introduce bulk quasiparticles with the fundamental charge.

SI12 Determination of the capacitance of the center gate from α-dependent AB interference

Fig. S11 summarizes the α-dependence of $\frac{\Phi_0}{\Delta B}$ for all fractional fillings in the current study as well as $\nu = \frac{1}{3}$ from our earlier experiment.[7] These results provide information on the CG capacitance. The constant-phase lines of the cosine in Eq. (S12) can be expressed as

$$\frac{\Phi_0}{\Delta B} = A\left(\nu_{LL} - \frac{e}{e_2^*}\frac{\tilde{\theta}_{12}}{2\pi}\nu\right) + A\left(\frac{e}{e_2^*}\frac{\tilde{\theta}_{12}}{2\pi}\frac{C_{\mathrm{CG}}\Phi_0}{e}\right)\frac{1}{\alpha}, \tag{S17}$$

where we used $e_1^* = \nu_{\mathrm{LL}}e$, $\tilde{\theta}_{12} = \theta_{12} - s_0$, and kept the dependence on the capacitance explicit. In particular, we use the CG capacitance C_{CG}, which can be different from the RG capacitance C_{RG}, denoted by C in the main text. The first term ('bias term') on the right-hand side of Eq. (S17) is independent of the capacitance. When e_2^* is the fundamental quasiparticle charge and bulk-edge couplings are absent, the factor $\frac{e}{e^*}\frac{\tilde{\theta}_{12}}{2\pi} = 1$. The intercept of $\frac{\Phi_0}{\Delta B}$ with the $\frac{1}{\alpha} = 0$ line in Fig. S11 thus directly quantifies how much $\tilde{\theta}_{12}$ deviates from the ideal case. The second term ('slope term') on the right-hand side of Eq. (S17) is proportional to C_{CG}. Fitting the measured data shown in Fig. S11 to a line thus determines both $\tilde{\theta}_{12}$ and C_{CG}

Table S1 summarizes the results of fitting the data for each filling factor. The significantly smaller value of C_{CG} for $\nu = \frac{1}{3}$ from the previous study can be explained by the different thicknesses of the top hBN, which was 48 nm for the previous study and 29 nm for the current study.

In Sec. SI2, we calculated C_{RG} = 0.959 mF/m^2 from the Landau fan diagram, which deviates from the C_{CG} values in Table S1 by 10% at $\nu = \frac{4}{3}$ and less than 7% at the other fillings. The actual difference between C_{RG} and C_{CG} is thus about half the value of 15% quoted in the main text, which did not take into account deviations $\tilde{\theta}_{12}$ from the theoretically expected value.

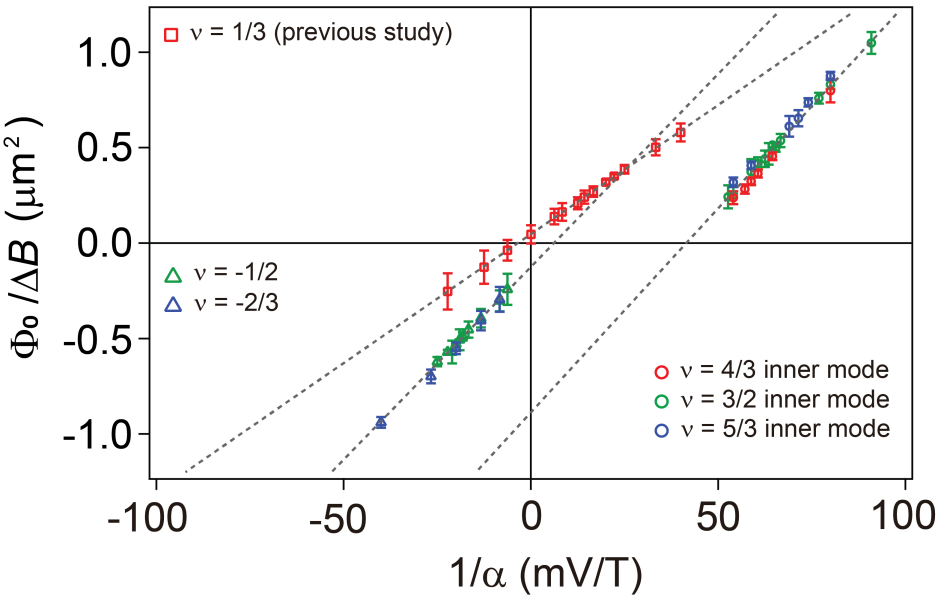

Figure S11: The statistical contribution to the interference of fractional quasiparticles. The magnetic field periodicity $\frac{\Phi_0}{\Delta B}$ obtained from 2D-FFTs is plotted as a function of $\frac{1}{\alpha}$ for the various fractional modes in the current study and the previous study.[7]

Table S1: Determination of the braiding phase $\tilde{\theta}_{12}$ and the capacitance of the center gate C_{CG}.

partitioned edge	A (μm²)	bias term (μm²)	slope term (Tμm²/mV)	$\frac{e}{e_2^*}\frac{\tilde{\theta}_{12}}{2\pi}$	C_{CG} (mF/m²)
ν = 4/3 inner mode	0.99 ± 0.10 (see SI7)	-0.967 ± 0.027	22.04 ± 0.43	0.98 ± 0.02	0.876 ± 0.017
ν = 3/2 inner mode		-0.887 ± 0.019	21.38 ± 0.28	0.93 ± 0.01	0.898 ± 0.011
ν = 5/3 inner mode		-0.843 ± 0.052	21.26 ± 0.77	0.91 ± 0.05	0.912 ± 0.033
ν = -1/2	1.02 ± 0.06 (see SI6)	-0.124 ± 0.009	20.21 ± 0.54	0.75 ± 0.01	1.013 ± 0.027
ν = -2/3		-0.136 ± 0.014	20.40 ± 0.60	0.80 ± 0.01	0.967 ± 0.028
ν = 1/3 (previous study)	1.00 ± 0.12	0.046 ± 0.001	13.52 ± 0.07	0.86 ± 0.01	0.607 ± 0.003

References for Supplementary Material

1. Venugopal, A. *et al.* Effective mobility of single-layer graphene transistors as a function of channel dimensions. *Journal of Applied Physics* **109** (2011).

2. Li, J. *et al.* Even-denominator fractional quantum Hall states in bilayer graphene. *Science* **358**, 648–652 (2017).

3. Kumar, R. *et al.* Quarter-and half-filled quantum Hall states and their competing interactions in bilayer graphene. *arXiv preprint arXiv:2405.19405* (2024).

4. Nakamura, J. *et al.* Aharonov-Bohm interference of fractional quantum Hall edge modes. *Nature Physics* **15**, 563–569 (2019).

5. Nakamura, J., Liang, S., Gardner, G. C. & Manfra, M. J. Impact of bulk-edge coupling on observation of anyonic braiding statistics in quantum Hall interferometers. *Nature Communications* **13**, 344 (2022).

6. Nakamura, J., Liang, S., Gardner, G. C. & Manfra, M. J. Direct observation of anyonic braiding statistics. *Nature Physics* **16**, 931–936 (2020).

7. Kim, J. *et al.* Aharonov–Bohm interference and statistical phase-jump evolution in fractional quantum Hall states in bilayer graphene. *Nature Nanotechnology* 1–8 (2024).